

# Spatial control of heavy-fermion superconductivity in CeIrIn<sub>5</sub>

Maja D. Bachmann<sup>1,2,†</sup>, G. M. Ferguson<sup>3,†</sup>, Florian Theuss<sup>3</sup>, Tobias Meng<sup>4</sup>, Carsten Putzke<sup>1,7</sup>, Toni Helm<sup>1</sup>, K.R. Shirer<sup>1</sup>, You-Sheng Li<sup>1,2</sup>, K.A. Modic<sup>1</sup>, Michael Nicklas<sup>1</sup>, Markus König<sup>1</sup>, D. Low<sup>3</sup>, Sayak Ghosh<sup>3</sup>, Andrew P. Mackenzie<sup>1,2</sup>, Frank Arnold<sup>1</sup>, Elena Hassinger<sup>1</sup>, Ross D. McDonald<sup>5</sup>, Laurel E. Winter<sup>5</sup>, Eric D. Bauer<sup>5</sup>, Filip Ronning<sup>5</sup>, B.J. Ramshaw<sup>3</sup>, Katja C. Nowack<sup>3,6\*,‡</sup> and Philip J.W. Moll<sup>1,7\*,‡</sup>

<sup>1</sup>Max-Planck-Institute for Chemical Physics of Solids, Dresden, D-01187 Germany

<sup>2</sup>School of Physics and Astronomy, University of St. Andrews, St. Andrews KY16 9SS, UK

<sup>3</sup>Laboratory of Atomic and Solid State Physics, Cornell University, Ithaca, NY 14853, USA

<sup>4</sup>Institute for Theoretical Physics, Technical University Dresden, D-01062 Dresden, Germany

<sup>5</sup>Los Alamos National Laboratory, Los Alamos, NM 87545, USA

<sup>6</sup>Kavli Institute at Cornell, Ithaca, New York 14853, USA

<sup>7</sup>Institute of Material Science and Engineering, École Polytechnique Fédéral de Lausanne (EPFL), 1015 Lausanne, Switzerland

\* To whom correspondence should be addressed: [philip.moll@epfl.ch](mailto:philip.moll@epfl.ch), [kcn34@cornell.edu](mailto:kcn34@cornell.edu)

†These authors contributed equally to this work.

‡These authors contributed equally to this work.

**Spatial control of the electronic properties of solids has led to landmark discoveries in condensed matter physics as well as new electronic applications. Although crystals of strongly correlated metals exhibit a diverse set of electronic ground states, few approaches to spatially modulating their properties exist. Here we demonstrate disorder-free control on the micron-scale over the superconducting state in samples of the heavy-fermion superconductor CeIrIn<sub>5</sub>. We pattern crystals on the micron-scale by focused ion beam milling to tailor the boundary conditions for the elastic deformation upon thermal contraction during cooling. The resulting non-uniform strain fields induce complex patterns of superconductivity due to the strong dependence of the transition temperature on the strength and direction of strain. Electrical transport and magnetic imaging of devices with various geometries reveal that the obtained spatial modulation of superconductivity matches predictions based on finite element simulations. These results showcase a generic approach to manipulating electronic order on micrometer length scales in strongly correlated matter without compromising the cleanliness, stoichiometry, or mean-free-path.**

The electronic ground state of heavy fermions sensitively depends on the coupling between a localized state and an itinerant electronic system. As the coupling strength is tuned, metallic, superconducting or magnetically ordered phases are induced yielding the rich phase diagrams typical for this materials class. This tunability could be exploited to generate new correlated behavior as well as device-based applications if the electronic order can be locally controlled within a crystalline sample. Metallic, magnetic or superconducting regions could be induced within a single crystal by precise spatial control over

the tuning parameter. Strain is a particularly powerful way to achieve this goal: it introduces no disorder and its independent components offer multiple degrees of freedom to couple to electronic order. Most commonly uniform uniaxial(1) or biaxial strain(2) is applied. Here, we demonstrate micron-scale control over the superconducting order in stoichiometric and ultra-clean CeIrIn<sub>5</sub> by inducing a non-uniform tailored strain field in microstructured single crystal devices. Our experimental approach is based on the interplay between strain induced by differential thermal contraction between the sample and the substrate, as well as sub-micron control over the shape of the sample. The tetragonal heavy-fermion metal CeIrIn<sub>5</sub> exhibits material parameters that are ideal for establishing spatial control of a correlated state (Sommerfeld coefficient  $\gamma \sim 720 \text{ mJ mol}^{-1} \text{ K}^{-2}$  (3), effective mass  $m^* \sim 30m_e$  (4)). The superconducting transition temperature,  $T_c$ , of this material is highly sensitive to strain, due to the strong dependence of Ce-4f hybridization on the Ce-Ce interatomic distance. Straining the sample along the  $a$ -direction increases the bulk superconducting transition temperature ( $T_{c0} = 400 \text{ mK}$ ) by  $56 \text{ mK/kbar}$ , while compression along the  $c$ -direction decreases it by  $-66 \text{ mK/kbar}$  (5, 6). Although uniaxial strain strongly alters  $T_c$ , the almost equal but opposite effects of  $a$ - and  $c$ -direction strain lead to an overall weak change of  $T_c$  under hydrostatic pressure ( $10 \text{ mK/kbar} \sim 2.5\% T_c/\text{kbar}$ ) (7). If a crystal is subjected to a non-uniform strain field, accordingly complex patches of superconductivity are expected to appear within the heavy Fermi liquid.

### **Non-uniform superconductivity within a single crystal**

Figure 1 illustrates non-uniform superconductivity for the simple case of a rectangular slab commonly referred to as lamella. The lamella ( $150 \times 30 \times 2 \mu\text{m}^3$ ) was carved from a macroscopic crystal using focused ion beam (FIB) machining (for fabrication details, see (8–10)) and joined to the sapphire substrate with a thin layer of epoxy (approximately a few hundred nanometers). This epoxy is significantly softer than the crystalline substrate and the sample; finite element modeling corroborates the intuitive assumption that the differential thermal contraction transmitted through the epoxy is largely independent of the exact details of the glue layer such as its thickness or elastic moduli (see (10) for details). The crystallographic  $c$ -direction is aligned with the short side of the lamella and the  $a$ -direction with the long side. Using (0001)-cut sapphire ensures isotropic thermal contraction of the substrate. While sapphire is known for its low thermal contraction, CeIrIn<sub>5</sub> contracts strongly upon cooling, as is typical of many Ce-based compounds (11). As a result, the sample is under tensile strain at low temperature.

To study the superconducting transition in the lamella, we use scanning superconducting quantum interference device (SQUID) microscopy (SSM) to

image the diamagnetic response of the sample with micrometer scale resolution. To detect superconductivity, we apply a local magnetic field using a  $\sim 6 \mu\text{m}$  field coil integrated on the SQUID chip while monitoring the local magnetic susceptibility with a  $\sim 1.5 \mu\text{m}$  SQUID pickup loop (see (10) for details). Superconducting regions of the sample exhibit a strong diamagnetic response, which enables us to distinguish them from metallic and insulating regions.

Susceptibility images as a function of temperature (Fig.1) reveal that superconductivity first emerges at the short edges, while most of the lamella remains metallic. As the temperature is lowered, larger fractions of the lamella become superconducting, leading to the growth of triangular superconducting patches protruding into the slab, which eventually join in the center (Fig. 1E). At even lower temperatures, the order parameter remains suppressed on the long edge. The observation of superconductivity at the edge of the sample before the interior is unexpected. Usually, for a thin superconducting slab cooled in the earth's magnetic field, the demagnetization factor at the sample edges favors the appearance of superconductivity in the center of the sample first (12).

Before analyzing the spatial pattern in the images, we estimate whether strain due to differential thermal contraction combined with the strain sensitivity of  $T_c$  in  $\text{CeIrIn}_5$  can cause the observed variations in  $T_c$  of several 100 mK. When cooled to cryogenic temperatures,  $\text{CeIrIn}_5$  and sapphire contract by  $\sim 0.3\%$  and  $\sim 0.08\%$  respectively. Given this mismatch, we expect strain on the order of  $0.1\%$  to exist within the  $\text{CeIrIn}_5$  crystal at low temperature. Previous studies of bulk single crystals (5, 6) indicate that  $\sim 0.1 \text{ GPa}$  ( $\sim 1 \text{ kbar}$ ) of uniaxial pressure changes  $T_c$  by 100 mK. Using a typical elastic modulus of 150 GPa, we estimate that compressive strains of  $\sim 0.1\%$  are achieved in these experiments. Both uniaxial pressure studies and the image series presented here are consistent with  $\sim 0.1\%$  strain generating  $\sim 100 \text{ mK}$  variation in  $T_c$ .

To understand the geometry in the images, we perform finite element method simulations of the strain field in the device caused by the difference in the thermal contraction between  $\text{CeIrIn}_5$  and sapphire (10). We then compute the local transition temperature,  $T_c$ , from the strain field using,

$$T_c = T_{c0} + \frac{\delta T_c}{\delta \epsilon_a} (\epsilon_a + \epsilon_b) + \frac{\delta T_c}{\delta \epsilon_c} \epsilon_c,$$

for each point on the grid resulting in a spatial  $T_c$  -map (Fig. 1 C). Here,  $\epsilon_i$  with  $i = a, b, c$  are the diagonal elements of the strain tensor along the corresponding crystallographic directions. We estimate  $\frac{\delta T_c}{\delta \epsilon_a} = -57 \text{ K}$  and  $\frac{\delta T_c}{\delta \epsilon_c} = 66 \text{ K}$  from reported bulk measurements of  $T_c$  as a function of uniaxial pressure, as well as

our measured elastic moduli (5, 6, 10). We generate binary images from this map marking superconducting and metallic regions at each temperature that can be directly compared to our susceptibility images (Fig. 1 D-F). We find detailed agreement between the spatial patterns of superconducting regions observed in the SSM images at various temperatures and the pattern predicted by the simulations which are free of fitting parameters. This agreement indicates that our modeling captures both the physical origin of the complex superconducting patches and the essence of the  $T_c$  modulation in the sample. Note that shear strains are not relevant to determine  $T_c$  for two reasons: (1) the shear strains are an order of magnitude smaller than the uniaxial strains in the lamella; (2) the symmetry of the superconducting order parameter in  $CeIrIn_5$  requires that shear strain couples to  $T_c$  at higher order than the uniaxial strains (see (10) for details). Comparison of the data and simulations show that including these higher-order couplings is not required to model the experimental results.

### **Induced strain field depends on geometry of FIB defined features**

Next, we show that the induced strain field and the shape of the superconducting regions can be tailored by using FIB micromachining. To define the strain field in the devices, additional trenches were cut through the lamella down to the substrate, changing the boundary conditions for the elastic equations. In both devices the trenches define a square in the  $(a,c)$ -plane (Fig.2). In device 1, the square is anchored by four constrictions in each corner (Fig. 2A). In device 2, the constrictions connect to the center of each side of the square (Fig. 2G). Under biaxial tension, each of the contact pads is pulled outwards, subjecting the square to non-uniform strain.

Device 1 is designed to measure anisotropic resistances in the plane by passing current through any pair of neighboring contacts, while measuring voltage across the remaining pair (13, 14). In this device, the simulated  $T_c$  map predicts a pattern of superconductivity first developing on the edges aligned with the  $c$ -direction as the device is cooled (Fig. 2 F). These regions extend towards the center upon lowering the temperature, eventually connecting in the middle of the device. Such patterns are evident in the SSM images (Fig. 2 B-D) and lead to three distinct regimes for transport through device 1: a) the normal state in which all contacts are separated by metallic regions, b) a state in which only the contact pairs along the  $c$ -direction are connected by superconducting regions, and c) a state in which all contacts are connected by a single superconducting region. As a result, when current is sourced between contacts along the  $c$ -direction (1 and 2), a transition to zero voltage signaling superconductivity at a relatively high temperature  $T_c^*$  is observed (Fig. 2 E, red trace). For currents sourced between contacts along the  $a$ -direction (2 and 4

we observe a sharp upturn in voltage along  $a$  as  $R_c$  goes to zero (Fig. 2 E, blue trace). The elongated superconducting regions identified in Figure 2D cause the current from contacts 2 to 4 to distribute evenly over the width of the device, leading to a larger current to flow at the voltage probes (1 and 3). Eventually, a second transition to a zero-resistance state occurs when all contacts are connected by a single superconducting region. The electrical response and the direct imaging of this device consistently capture the key concepts of the microscopic control over correlations: two directed superconducting paths form in a chemically homogeneous metal following the imprinted strain profile.

In contrast to device 1, the edges in device 2 parallel to the  $a$ -axis superconduct well before the central region of the device (Fig. 2 G-K). As with device 1, we find that simulations of the strain profile in the device reproduce the structure of the superconducting transition in detail. The contrast between the two image series indicates that the structure in the images is determined by the interplay between the intrinsic strain sensitivity of the material and the strain field imposed by the FIB defined features.

In device 2, we observe a pronounced suppression and enhancement of  $T_c$  in the  $a$ - and  $c$ - aligned constrictions respectively. The strain in the constrictions is enhanced because the contact pads on one side and the square on the other side exert forces on the constrictions that point outwards. This observation suggests a strategy to design devices that exhibit a strong modulation of  $T_c$  and to generate confined regions of suppressed superconductivity.

### **Large tunability of $T_c$ in small structures**

Smaller devices exhibit an even more pronounced dependence of the transport  $T_c$  on their geometry than larger devices. Device 3 features three series-connected straight beams with dimensions  $22 \times 1.7 \times 8 \mu\text{m}^3$ , with two beams aligned with the  $c$ - and one with the  $a$ -direction (Fig. 3A). These fine structures cannot be resolved in detail with SSM. In transport, the transition temperature for the  $c$ -aligned beam  $T_c^c \sim 700 \text{ mK}$  is higher than the bulk  $T_c$ , while the transition temperatures for the  $a$ -aligned beams  $T_c^a \sim 200 \text{ mK}$  are significantly lower than the bulk  $T_c$ . Additional small structures show equally or even more dramatic variations of  $T_c$  (10). Therefore, a modulation of the transition temperature by more than a factor of 4 within a single crystal can be realized within our fabrication approach.

### **High critical currents**

To exploit strain tuning of the superconducting order for future device-based experiments, the superconducting state must remain robust after device

fabrication. In order to estimate the critical current of each beam, we apply high currents to device 3 (Fig. 4 A,B). The current is increased until an observable voltage signals the breakdown of the zero-resistance state. To minimize self-heating, rectangular current pulses 83  $\mu$ s in duration are applied to the sample with a cooldown time between pulses of 100 ms. Because the critical current decreases monotonically with increasing temperature, the obtained values represent a lower bound of their magnitude in the absence of heating. Figure 4A shows a typical current-voltage characteristic of the c-aligned beam at 500mK, well above the bulk  $T_c$ . A robust zero resistance state is detected up to a critical current density of about 12.5 kA cm<sup>-2</sup>. Upon cooling, the critical current density increases to  $j_c^c$  (0K)  $\sim$  18 kA cm<sup>-2</sup> (Fig. 4B). This high critical current is typical for bulk heavy fermion superconductors (UPt<sub>3</sub>  $\sim$ 3.8 kA cm<sup>-2</sup>, ref.(15); URu<sub>2</sub>Si<sub>2</sub>  $\sim$ 24 kA cm<sup>-2</sup>, ref.(15); CeCu<sub>2</sub>Si<sub>2</sub>  $\sim$ 1-5 kA cm<sup>-2</sup>, ref.(16)), strongly supporting a scenario of robust, bulk-like superconductivity over the formation of sparse superconducting filaments under strain.

Incidentally, our observations answer an open question in CeIrIn<sub>5</sub> about the origin of the commonly observed discrepancy between thermodynamic and resistive measurements of  $T_c$  in CeIrIn<sub>5</sub>. Bulk crystals display a transition to a zero-resistance state well above  $T_c$ , starting as high as  $T_c^* \sim 1.2$  K (17–19) dependent on the details of the sample. Our results microscopically confirm proposals that strain fields around defects induce this 1K-phase (20–22). In particular, the upper critical fields  $H_{c2}$  of the strain-induced superconductivity in the microdevices can be directly scaled onto the bulk values (Fig. 3 C-E). This critical field scaling was experimentally identified early-on in macroscopic crystals as a hallmark signature of the 1K phase (3). Based on these observations, we propose that the 1K phase is a strain effect arising from crystal handling and wiresawing. To directly test this hypothesis, we prepared macroscopic samples by wiresaw cutting. While all these samples initially had a  $T_c > 1$  K, the resistive signatures of this 1K-phase are completely removed by short surface etching in HCl, after which the resistive transition coincides with thermodynamic probes at  $T_c \sim 400$  mK (10). This result demonstrates the absence of defect-strained superconducting patches in good single crystals of CeIrIn<sub>5</sub> and establishes the discrepancy between thermodynamic and resistive measurements of  $T_c$  in CeIrIn<sub>5</sub> as an effect of surface strain.

## Discussion and outlook

Here, we report a strategy to spatially modulate superconductivity within a clean electronic system that is induced by strong, non-trivial strain patterns. Spatial gradients of  $T_c$  have been generated by other methods, for example by modulating the chemical potential across the sample by gradient-doping using molecular-beam epitaxy techniques (23). In this method variations in the

local charge carrier density modifies the local transition temperature. In the stoichiometric CeIrIn<sub>5</sub> microstructures studied here, the charge carrier density is uniform as evidenced by unperturbed quantum oscillations in device 3 (Fig. 4C-E). These quantum oscillations quantitatively match the angle dependence of previously reported de Haas-van Alphen oscillations (4) measured on macroscopic crystals and indicate that the Fermi surface shape remains unchanged by the weak strain field. In particular, the large, heavy orbits and their fine structure are readily observed which is usually very difficult in transport. This observation is incompatible with the presence of strong charge carrier density changes across the sample, which would lead to spatial variations in the Fermi surface cross-sections and subsequently suppress quantum oscillations by phase smearing.

At the same time, the strain fields in device 3 are strong enough to modulate  $T_c$  by almost a factor of 4, from 200 mK to 780 mK. This finding suggests that the strain field spatially modulates the degree of 4f-hybridization across the device, and thereby  $T_c$ . This mechanism - which is at first surprising - is compatible with experimental observations in the related compound CeRhIn<sub>5</sub> in which hydrostatic pressure suppresses anti-ferromagnetism and eventually induces superconductivity. Despite the significant changes in the 4f-magnetism and the spin fluctuation spectrum, the quantum oscillation frequencies remain completely unchanged in the entire pressure range up to the quantum critical point (24). However, the 4f-hybridization increases as evidenced by the growing quasiparticle effective mass upon applying pressure. This strongly supports that the hybridization with the 4f electrons varies without changes in the overall volume of the Fermi surface. Here we propose that the same microscopic physics underlies the spatial modulation of  $T_c$  in CeIrIn<sub>5</sub> microstructures.

In general, strongly correlated materials exhibit a pronounced sensitivity to perturbations, owing to the small energy scales defining their physics. The strain accessible by our fabrication approach is sufficient to substantially alter the electronic properties of these materials (27), without introducing chemical disorder. Unlike chemical approaches to tune correlations, the FIB provides micrometer scale control over both the direction and magnitude of the induced strain field. We expect that the approach demonstrated here will enable spatial control of a wide range of broken symmetry states in strongly correlated systems. We envision clean interfaces between regions with different electronic order within a sample generated by a spatially modulated strain field, e.g. by generating antiferromagnetic/superconducting structures in strained CeRhIn<sub>5</sub> (24). Further, this approach is immediately compatible with any material that can be patterned using a FIB, paving the way for a range of new experiments on strongly correlated matter. Importantly, while we focus on

devices aligned along specific crystal axes, devices can be oriented along any direction to generate strain patterns of any desired symmetry. Our approach to fabricating complex superconducting structures within a clean single crystal can stimulate both new fundamental and applied research. For example, strain engineering may offer an alternative way to fabricate superconducting circuitry within a metallic layer without any physical junctions, providing a surprising new route to fabricating S/N/S Josephson junctions within a single crystal.

## References

1. C. W. Hicks *et al.*, Strong Increase of  $T_c$  of  $\text{Sr}_2\text{RuO}_4$  Under Both Tensile and Compressive Strain. *Science*. **344**, 283–285 (2014).
2. A. E. Böhmer *et al.*, Effect of Biaxial Strain on the Phase Transitions of  $\text{Ca}(\text{Fe}_{1-x}\text{Co}_x)_2\text{As}_2$ . *Phys. Rev. Lett.* **118**, 107002 (2017).
3. C. Petrovic *et al.*, A new heavy-fermion superconductor  $\text{CeIrIn}_5$ : A relative of the cuprates? *Europhys. Lett.* **53**, 354–359 (2001).
4. Y. Haga *et al.*, Quasi-two-dimensional Fermi surfaces of the heavy fermion superconductor  $\text{CeIrIn}_5$ . *Phys. Rev. B*. **63**, 060503R (2001).
5. O. M. Dix *et al.*, Anisotropic Dependence of Superconductivity on Uniaxial Pressure in  $\text{CeIrIn}_5$ . *Phys. Rev. Lett.* **102**, 197001 (2009).
6. N. Oeschler *et al.*, Uniaxial Pressure Effects on  $\text{CeIrIn}_5$  and  $\text{CeCoIn}_5$  Studied by Low-Temperature Thermal Expansion. *Phys. Rev. Lett.* **91**, 076402 (2003).
7. R. Borth *et al.*, Heat capacity of the heavy fermion superconductor  $\text{CeIrIn}_5$  under hydrostatic pressure. *Phys. B Condens. Matter*. **312–313**, 136–137 (2002).
8. P. J. W. Moll *et al.*, Field induced density wave in the heavy fermion compound  $\text{CeRhIn}_5$ . *Nat. Commun.* **6**, 6663 (2015).
9. F. Ronning *et al.*, Electronic in-plane symmetry breaking at field-tuned quantum criticality in  $\text{CeRhIn}_5$ . *Nature*. **548**, 313–317 (2017).
10. See supplementary material.
11. R. S. Kumar *et al.*, Anisotropic elastic properties of  $\text{CeRhIn}_5$ . *Phys. Rev. B*. **69**, 014515 (2004).
12. M. Tinkham, *Introduction to Superconductivity* (Dover Publications, 2004).
13. H. C. Montgomery, Method for measuring electrical resistivity of anisotropic materials. *J. Appl. Phys.* **42**, 2971–2975 (1971).



14. L. J. van der Pauw, A method of measuring the resistivity and Hall coefficient on lamellae of arbitrary shape. *Philips Tech. Rev.* **20** (1958), pp. 220–224.
15. S. Wüchner, N. Keller, J. L. Tholence, J. Flouquet, Magnetic properties of the heavy-fermion superconductors UPt<sub>3</sub> and URu<sub>2</sub>Si<sub>2</sub>. *Solid State Commun.* **85**, 355–360 (1993).
16. A. Pollini *et al.*, Flux dynamics and low-field magnetic properties of the heavy-fermion superconductor CeCu<sub>2</sub>Si<sub>2</sub>. *J. Low Temp. Phys.* **90**, 15–53 (1993).
17. H. Shishido *et al.*, Fermi surface, magnetic and superconducting properties of LaRhIn<sub>5</sub> and CeTln<sub>5</sub> (T: Co, Rh and Ir). *J. Phys. Soc. Japan.* **71**, 162–173 (2002).
18. T. Shang *et al.*, CeIrIn<sub>5</sub>: Superconductivity on a magnetic instability. *Phys. Rev. B - Condens. Matter Mater. Phys.* **89**, 041101R (2014).
19. S. Nair *et al.*, Analysis of the normal-state magnetotransport in CeIrIn<sub>5</sub>. *J. Supercond. Nov. Magn.* **22**, 195–199 (2009).
20. S. Wirth *et al.*, Structural investigations of CeIrIn<sub>5</sub> and CeCoIn<sub>5</sub> on macroscopic and atomic length scales. *J. Phys. Soc. Japan.* **83**, 061009 (2014).
21. S. Nair *et al.*, Precursor state to superconductivity in CeIrIn<sub>5</sub>: Unusual scaling of magnetotransport. *Phys. Rev. B - Condens. Matter Mater. Phys.* **79**, 094501 (2009).
22. A. Bianchi *et al.*, Origin of the zero-resistance anomaly in heavy fermion superconducting CeIrIn<sub>5</sub>: A clue from magnetic-field and Rh-doping studies. *Phys. Rev. B.* **64**, 220504R (2001).
23. J. Wu, I. Božović, Perspective: Extremely fine tuning of doping enabled by combinatorial molecular-beam epitaxy. *APL Mater.* **3**, 062401 (2015).
24. H. Shishido, R. Settai, H. Harima, Y. Onuki, A Drastic Change of the Fermi Surface at a Critical Pressure in CeRhIn<sub>5</sub>: dHvA Study under Pressure. *J. Phys. Soc. Japan.* **74**, 1103–1106 (2005).

**Acknowledgments:** We are very grateful for the interesting and stimulating discussions with S. Kivelson, J. Zaanen, J. Tranquada, M. Vojta, P. Fulde, J. Thomson, S. Wirth, M. Sigrist, C. Geibel, H. von Löhneysen. We thank N. Nandi for the low temperature measurements.

**Funding:** Work at the Max Planck Institute of Chemical Physics of Solids was supported by the Max-Planck-Society and funded by the Deutsche Forschungsgemeinschaft (DFG, German Research Foundation) – MO 3077/1-1. Work at Cornell University was primarily supported by the Department of Energy, Office of Basic Energy Sciences, Division of Materials Sciences and Engineering, under Award DE-SC0015947 (scanning SQUID imaging, implementation of mK microscope). Support by the Cornell Center of Materials Research with funding from the NSF MRSEC program under Award DMR-1719875 (SQUID and microscope design) is also

acknowledged. TM is supported by the Deutsche Forschungsgemeinschaft through SFB 1143 and the Emmy Noether-Programme via grant ME 4844/1-1. M.D.B. acknowledges studentship funding from EPSRC under grant no. EP/I007002/1. P.J.W.M. was supported by the European Research Council (ERC) under the European Union's Horizon 2020 research and innovation programme (GA N° 715730). Work at Los Alamos National Laboratory was performed under the auspices of the US Department of Energy, Office of Basic Energy Sciences, Division of Materials Sciences and Engineering.

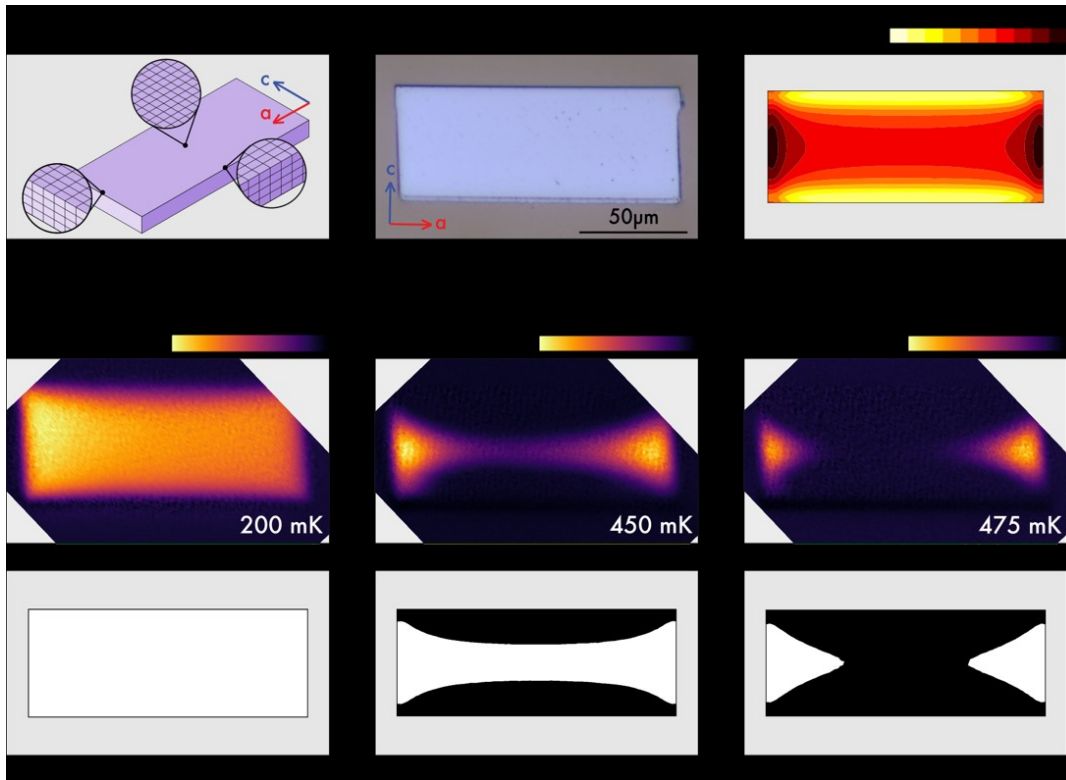
**Author contributions:** M.D.B, K.A.M., M.K., C.P., P.J.W.M. fabricated the microstructures, M.D.B., T.H., K.R.S. K.A.M., Y.-S.L., M.N., C.P., P.J.W.M. performed the transport measurements and G.M.F. performed the scanning SQUID imaging with support from D.H.L. and K.C.N.. F.T. and G.M.F. performed the finite element simulations with input from K.C.N. and B.J.R.. The crystals were grown by E.D.B and F.R. T.M. contributed the theoretical treatment of a 1D pairing. F.A., E.H., M.D.B. performed the magneto-transport measurements in the dilution refrigerator. R.D.M. and L.W. measured simultaneous transport in liquid  $^3\text{He}$ . All authors were involved in the design of the experiment and writing of the manuscript.

**Data availability:** All data needed to evaluate the conclusions in the paper are present in the paper. Additional data related to this paper may be requested from the authors. All data underpinning this publication can be accessed in comprehensible ASCII format at the pure research information system of the University of St Andrews at [www.st-andrews.ac.uk/staff/research/pure](http://www.st-andrews.ac.uk/staff/research/pure).

**Supplementary information:** Additional data supporting this manuscript are available online. The supplement contains the following subsections: Single-crystal growth; FIB fabrication; Crystalline quality of the microstructures; Reproducibility; Susceptibility images; Finite element method simulations; Measurements of  $\text{CeIrIn}_5$  elastic moduli.

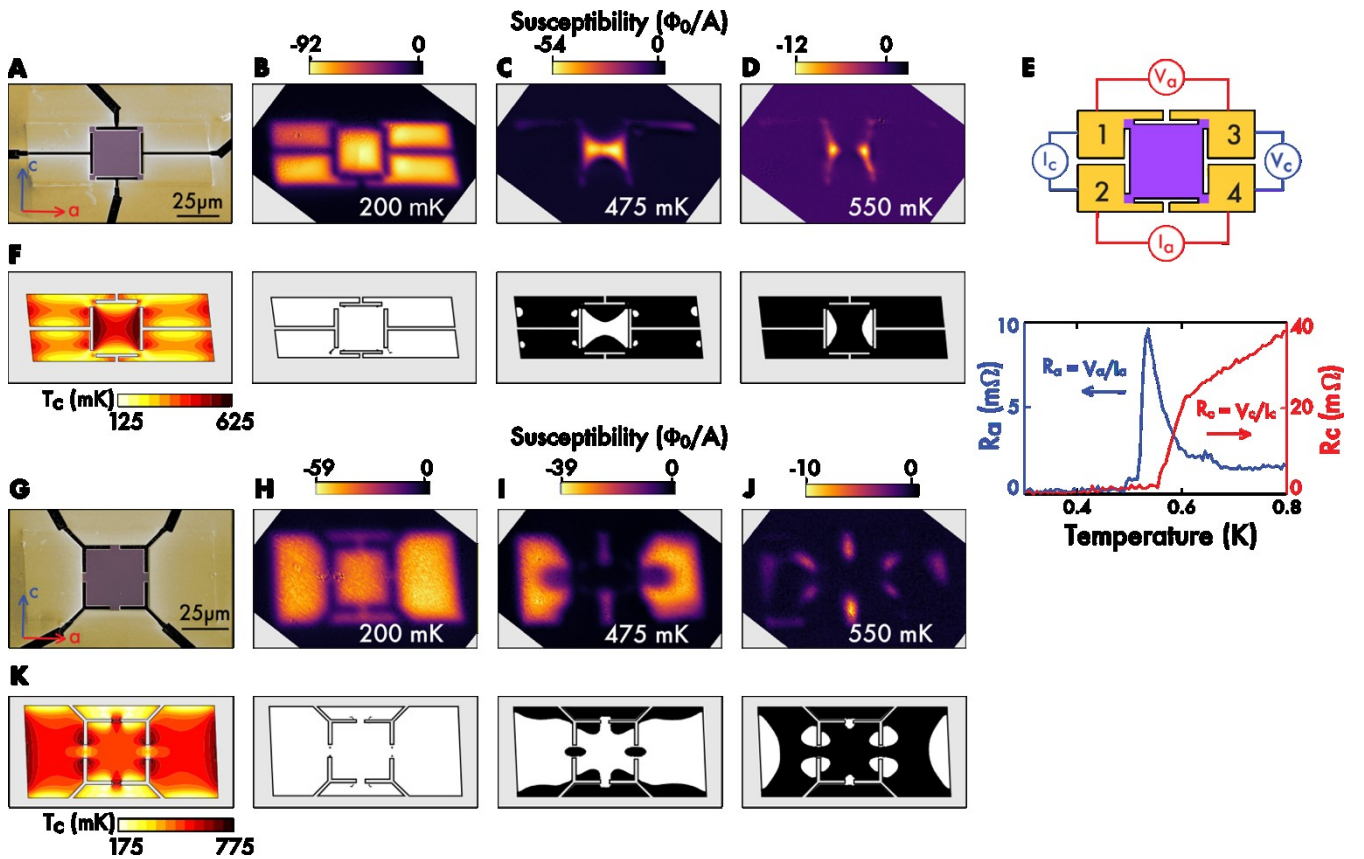
## Figures

Figure 1: The superconducting transition in a slab under biaxial strain



- A) Sketch of the distortion of a thin slab of  $\text{CeIrIn}_5$  coupled to sapphire at low temperatures.
- B) Optical image of a slab  $2 \mu\text{m}$  in thickness cut by FIB machining in the  $(a,c)$  plane.
- C)  $T_c$ -map across the sample arising from the strain profile and the strain-dependence of  $T_c$  estimated from finite element simulations.
- D) – F) Top: Local susceptibility images at three representative temperatures. A negative diamagnetic susceptibility indicates superconducting regions of the sample. Bottom: Superconducting regions (white) calculated from the strain profile in the device. The calculated regions correspond to constant temperature contours of the  $T_c$ -map in (C).

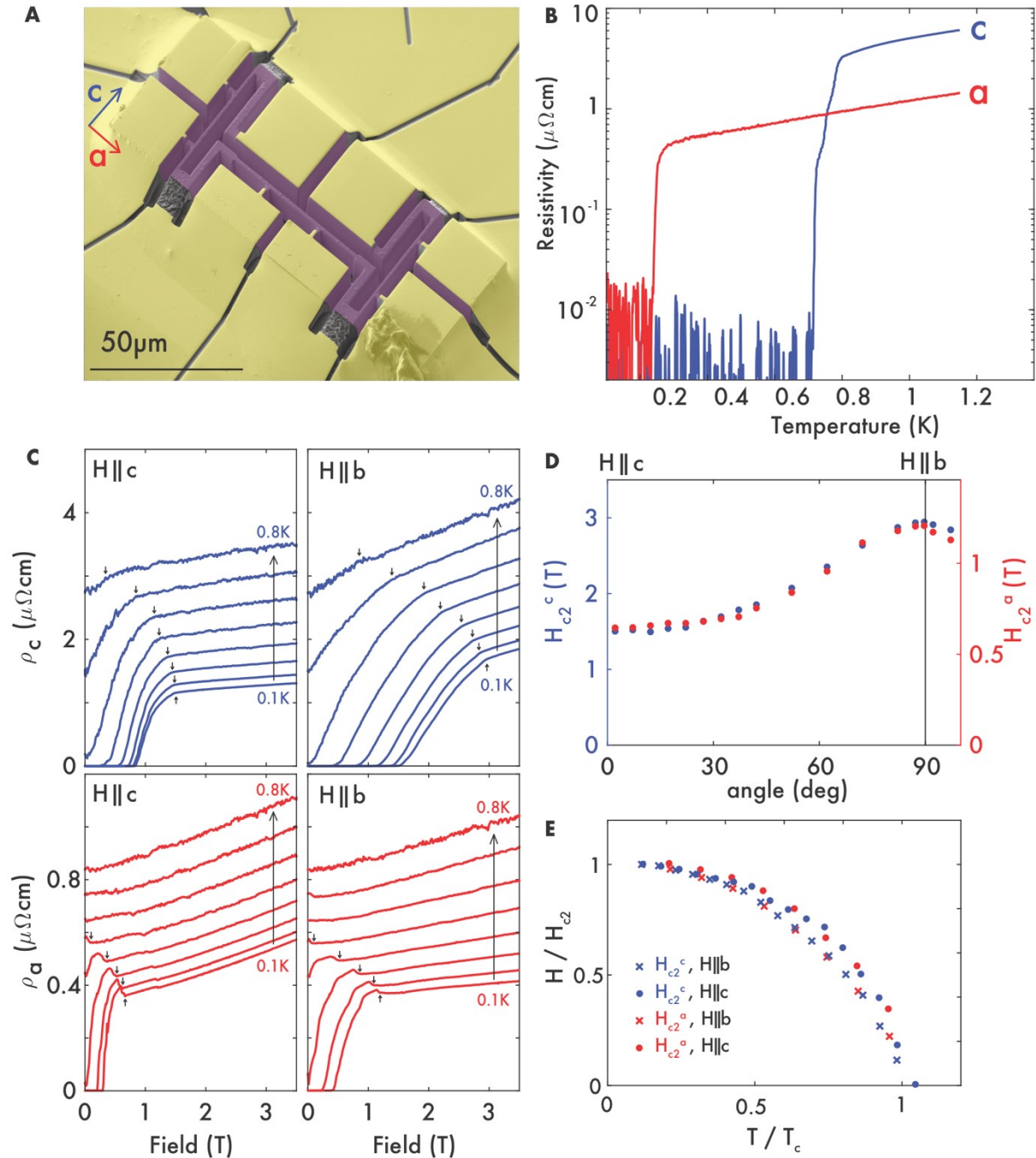
Figure 2: Spatial control over correlations



- A) Scanning electron microscopy image of device 1. The slab is FIB-cut in the (a,c) plane and contacted by evaporated Au (yellow). The center square of the device is  $25 \times 25 \times 3 \mu\text{m}^3$ , held by contacts in the corners. The scale bar is  $25 \mu\text{m}$ .
- B) – C) Local susceptibility images at three representative temperatures illustrate the temperature evolution of the spatially modulated superconducting state. Lower panels show calculated superconducting patterns.
- E) Montgomery transport measurement upon cooling of device 1. As the first superconducting regions appear along the sides along the c-direction (D), the c-direction resistance  $R_c = \frac{V_{12}}{I_{34}}$  vanishes and the a-direction resistance  $R_a = \frac{V_{13}}{I_{24}}$  experiences a voltage spike, due to a sudden current redistribution. At lower temperatures, these regions touch (C), leading to zero resistance across all contacts.
- F)  $T_c$ -map from finite element calculations.
- G) Scanning electron microscopy image of device 2. The fabrication of device 2 was as similar as possible to that of device 1, but with the constrictions connecting at the middle of each side of the square, not the corners (compare with A).
- H) - K) The same as in (A-F), but for device 2. A completely different

superconducting pattern unfolds, as expected from the difference in position of the contacts.

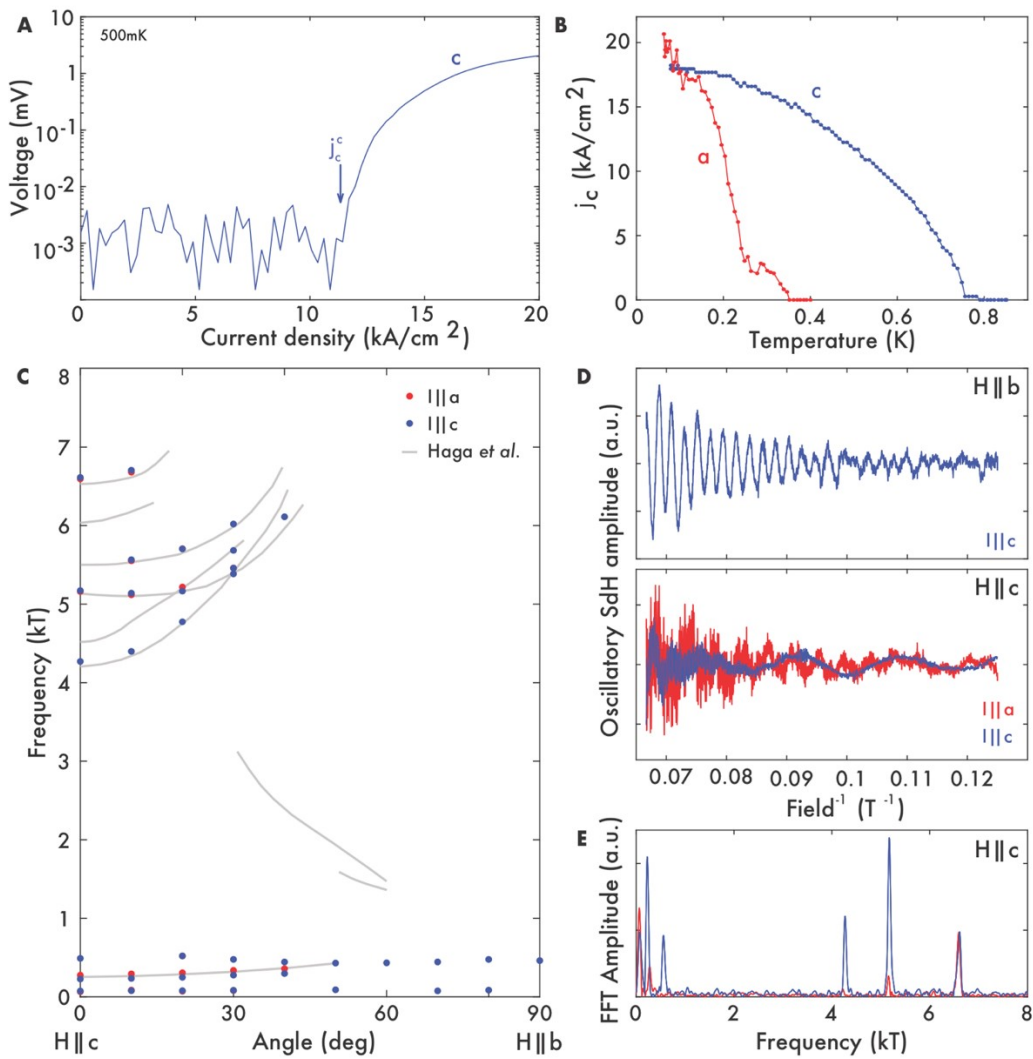
**Figure 3: Smaller structures**



(A) Scanning electron microscopy image of device 3. The device consists of long bars of dimension  $(1.8 \times 8 \times 22 \mu\text{m}^3)$ . Two bars are oriented along the  $c$ -direction and one along the  $a$ -direction.

- (B) Resistivity as a function of temperature for device 3. Strain suppresses  $T_c$  along the bar aligned with the crystallographic  $a$ -axis and enhances  $T_c$  along bars aligned with the  $c$ -axis.
- (C) Temperature-dependent magnetoresistance along the  $a$ - and  $c$ -direction in  $\text{CeIrIn}_5$  for different field orientations. All measurements were taken in a full-Lorentz-force configuration except  $\rho_c, H \parallel c$ , which is naturally longitudinal.
- (D) Angle dependence of the critical fields defined as the points where deviation from the normal magnetoresistance occurs (arrows in A), for both current configurations. The data collapse onto a single curve by scaling (compare the two vertical axes).
- (E) Temperature dependence of the critical fields for all four current and field configurations. The curves for each field configuration collapse when scaled by the respective values of  $H_{c2}(0\text{ K})$  and  $T_c$  using the experimental values for in-plane transport ( $T_c \sim 0.45\text{ K}$ ,  $H_{c2}^a \parallel b(0\text{ K}) \sim 1.2\text{ T}$ ,  $H_{c2}^a \parallel c(0\text{ K}) \sim 0.65\text{ T}$ ) and along the  $c$ -direction ( $T_c^* \sim 0.8\text{ K}$ ,  $H_{c2}^{*,c} \parallel b(0\text{ K}) \sim 2.95\text{ T}$ ,  $H_{c2}^{*,c} \parallel c(0\text{ K}) \sim 1.5\text{ T}$ ).

**Figure 4: Robust superconductivity coexists with quantum oscillations**



- (A) Current/voltage characteristic along the  $c$ -direction measured on the device shown in Figure 3A. The onset of measurable voltage above the experimental noise level was used to define  $j_c^a$  and  $j_c^c$  (arrow).
- (B) Critical current along both directions. A robust, high- $j_c$  state is observed along the  $c$ -direction whereas the  $a$ -direction is in a metallic state.
- (C) Angle dependence of Shubnikov-de Haas (SdH) oscillations at 80 mK measured in device 3 (points) overlaid on de Haas-van Alphen oscillations measured on bulk single crystals (grey lines).
- (D) SdH oscillation in the microstructure for H||b (top) and H||c (bottom).
- (E) The fast Fourier transform spectrum for the oscillations in (D).